Side-Firing Fiber Device for Underwater Tissue Ablation with Ho:YAG and Er:YAG Laser Radiation

Oliver Föhn,[†] Hans S. Pratisto,[†] Flurin Könz,[†] Michael Ith,[†] Hans J. Altermatt,[‡] Martin Frenz,[†] and Heinz P. Weber[†]

[†]University of Bern, Institute of Applied Physics, Sidlerstrasse 5, CH-3012 Bern, Switzerland;
[‡]University of Bern, Pathological Institute, Sidlerstrasse 5, CH-3012 Bern, Switzerland

ABSTRACT

A side-firing fiber device for arthroscopic Ho:YAG ($\lambda = 2.12$ μm) and Er:YAG ($\lambda = 2.94$ μm) laser applications was designed and constructed. The fiber delivery instrument consisted of a zirconium fluoride (ZrF_4) fiber equipped with a coaxially mounted short end-piece of low OH^- quartz fiber polished at an angle of 30 deg. The dynamics and depth of the vapor channel in water and the amplitude of pressure transients associated with the collapse of the vapor channel were measured for pulse energies up to 1 J (Ho:YAG) and 200 mJ for the Er:YAG laser (pulse duration $\tau = 400$ μs), respectively. To assess the feasibility of the side-firing fiber delivery instrument, the ablation efficiency and laser-induced damage in poly(acylamide) and meniscal tissue were determined after Ho:YAG and Er:YAG laser ablation. © *1998 Society of Photo-Optical Instrumentation Engineers.* [S1083-3668(98)00601-7]

Keywords pulsed infrared laser; arthroscopic surgery; cavitation; vapor bubble; acoustic transient.

1 INTRODUCTION

Ho:YAG and Er:YAG lasers emitting at 2.12 and 2.94 μm, respectively, are ideally suited for tissue treatment because these wavelengths are strongly absorbed in water. The absorption coefficient was reported to be 25 to 35 cm^{-1} for 2.12 μm and around 10^4 cm^{-1} for 2.94 μm, corresponding to an optical penetration depth of 285 to 400 μm and 1 μm, respectively.[1,2] Combined with a fiber delivery system, these wavelengths could become the choice for microsurgical endoscopic procedures in orthopedics, ophthalmology, otorhinolaryngology or gynecology.[3–7] While standard low OH^- fibers transmit 2.12-μm laser radiation with an acceptable attenuation (~ 0.07 dB/m), they are not sufficiently transparent to guide 2.94-μm laser radiation (≈ 100 dB/m). Sapphire, fluoride, and silver halogenide fibers or hollow wave guides are known light guides for transmitting 2.94-μm radiation.[8–10] Among these, the zirconium fluoride (ZrF_4) fibers seem to be the most promising (≈ 0.1 dB/m attenuation at 2.94 μm). The brittle and hygroscopic properties of the (ZrF_4) fiber, however, require protection against mechanical destruction and contamination of aqueous solutions.[11]

Today's operation procedures in orthopedic surgery (e.g., meniscectomy or smoothing of cartilage) take place in a liquid environment.[12,13] Underwater tissue treatment with infrared radiation is accompanied by the formation of vapor bubbles that act as transmission channels for the IR laser radiation between the fiber tip and the tissue surface.[14,15] The formation and the collapse of these bubbles, however, is accompanied by the generation of pressure transients[16–18] that can lead to mechanical tissue damage and/or destruction of the delivery instrument. An additional complication of endoscopic orthopedic procedures is that the freedom of movement in the joint is limited to a few millimeters, and the tissue surface that has to be irradiated is often not in an axial direction to the fiber applicator.

The aim of this study was to investigate the performance of a side-firing fiber device for 2.12- and 2.94-μm laser radiation that is best adapted to the specific requirements found in arthroscopic knee surgery. To evaluate the energy threshold for bubble formation at the side-firing fiber tip, transmission experiments with the aiming beam of an He:Ne laser were performed. Simultaneously used flash videography and pressure measurements allowed us to estimate the probability of undesired mechanical damage of the fiber system and in the tissue. In addition, we attempted to determine and to compare the tissue response in human meniscus after Ho:YAG and Er:YAG laser ablation *in vitro*.

Address all correspondence to Martin Frenz. Tel.: 4131 631 8943; Fax: 41 31 631 3765; E-mail: frenz@iap.unibe.ch
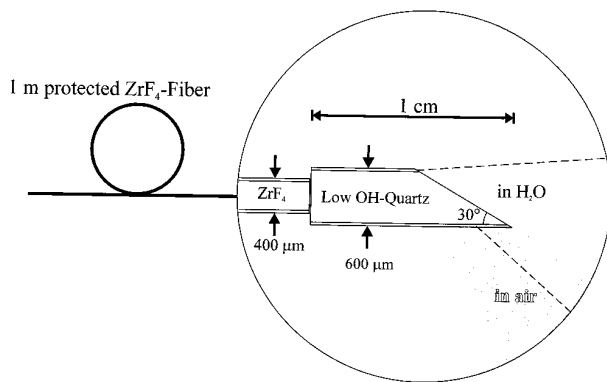
Fig. 1 Scheme of the side-firing fiber device. The broken lines in front of the side-firing fiber tip indicate the borders of the beam propagation under water. The shaded area indicates the zone of the beam propagation in air.

2 MATERIALS AND METHODS

2.1 LASER SYSTEM

An Ho:YAG ($\lambda = 2.12 \, \mu$m) and an Er:YAG ($\lambda = 2.94 \, \mu$m) laser rod with a diameter of 4 mm and a length of 80 mm were flashlamp pumped in an elliptical cavity.[19] Both lasers were operated in a free-running multimode at a pulse repetition rate of 2 Hz. The pulse duration was 400 μs (full length). A detailed description of the experimental setup of the multiwavelength laser system used has been published elsewhere.[20] The beams of both lasers were collinearly combined using an Infrasil prism and coupled into a ZrF$_4$ fiber (Le Verre Fluore) with a core diameter of 350 μm by a CaF$_2$ lens ($f = 50$ mm). Because of the brittleness of ZrF$_4$, the fiber was covered over its entire length by a flexible plastic tube. The distal surface of the fiber was protected by a 1-cm piece of low-OH$^-$ quartz fiber (core diameter 540 μm). The quartz piece was polished at an angle of 30 deg. A schematic drawing of the side-firing fiber device is shown in Figure 1. The total energy transmission for both laser wavelengths from the outcoupling mirror to the distal fiber end was 65%. The attenuation is mainly induced by the index mismatch at the interfaces. The maximum pulse energy at the fiber tip amounted to 1000 and 200 mJ for the Ho:YAG and the Er:YAG lasers, respectively. Lower pulse energies were achieved by introducing thin absorbing glass slides into the laser beam in front of the incoupling lens. The combination of a long ZrF$_4$ fiber for low loss transmission of radiation and of a short quartz fiber tip for protection and beam shaping (the fiber tip can be angled, conical, or ball shaped) represents a universal delivery system optimally adaptable to almost all medical requirements.

2.2 BEAM PATH, IMAGING OF BUBBLE FORMATION, AND PRESSURE MEASUREMENTS

The beam path through the fiber tip was calculated with geometrical optics for two cases: (1) with air

Table 1 Indices of refraction in different materials for wavelengths of 2.12 and 2.94 μm.

Index	$\lambda = 2.12 \, \mu$m	$\lambda = 2.94 \, \mu$m
n (air)	1	1
n (water)	1.29	1.28
n (quartz)	1.43	1.42

around the fiber tip and (2) with the fiber tip submerged in water. The indices of refraction of the different materials and wavelengths used are summarized in Table 1.[2,21] The beam diameter of the radiation propagating in air was measured from impacts on black absorbent photo paper.

The starting point of the vapor bubble formation in water was determined by a transmission experiment using He:Ne laser radiation. The experimental setup is shown in Figure 2. An Infrasil prism (prism angle of 72°) was used to couple the He:Ne laser beam simultaneously with 2.12- and 2.94-μm radiation into the fiber. The side-firing fiber tip was placed in a cuvette filled with distilled water. A photodiode at the bottom of the cuvette detected the He:Ne light exiting the fiber coaxially. The maximum signal of the photodiode indicated that the He:Ne beam pointed in an axial direction and the minimum signal indicated that a vapor bubble in front of the fiber tip was completely formed. The vapor bubble induces a change in the index of refraction at the interface that causes the beam to become totally internally reflected, leading to deflection sideways out of the fiber.

The formation and the shape of the laser-induced vapor bubble at the submerged side-firing fiber tip was monitored by time-resolved flash videography (schlieren illumination technique). The flashlamp [$\tau = 40$ ns at full-width half-maximum (FWHM)]

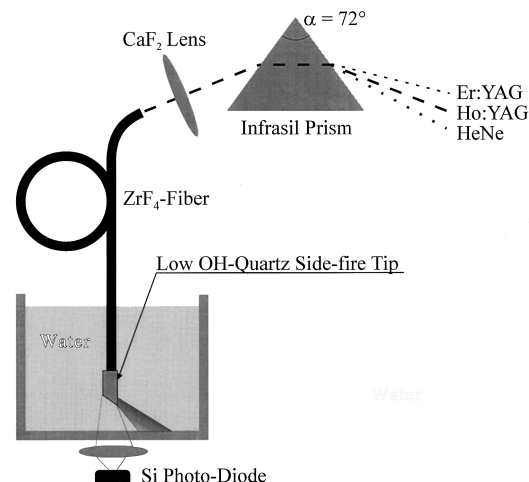**Fig. 2** Setup of the He:Ne laser transmission experiment.

was triggered at a predetermined time delay between 5 and 1000 μs after the beginning of the laser pulse. The images were captured with a standard CCD camera and recorded on videotape. The drilling depth of a bubble generated at the side-firing fiber tip was defined as the depth measured perpendicular to the fiber axis. The maximum size of the bubble was determined by varying the delay of the illuminating flashlamp. The pictures were loaded to a computer via a frame grabber unit for further analysis.

The pressure transients associated with the bubble formation and collapse were measured with a piezoelectric polyvinylidene fluoride (PVDF) needle hydrophone. The active diameter of the probe was 0.5 mm and its rise time amounted to 30 ns. The hydrophone tip was placed at the same depth as the side-firing fiber tip at a distance of 2 mm perpendicular to the fiber axis. For qualitative pressure measurements, a low noise amplifier with a bandwidth of 1 MHz was used (maximum gain factor of 100). In order to use the full bandwidth of the needle hydrophone, absolute pressure measurements were performed without an amplifier. The signals were stored on a digital oscilloscope. The measured pressure amplitudes were extrapolated up to the collapse center ($r = 100$ μm) assuming that the amplitude of a spherical acoustic wave is inversely proportional to the distance r from the center.[22,23]

2.3 TISSUE TREATMENT

Poly(acrylamide) gels with a water concentration of 80% were used as tissue phantoms.[17,24] They are optically transparent, which allows one to investigate the dynamics of the ablation process. The submerged distal side-firing fiber tip was placed at an angle of 46 deg relative to the gel surface. The fiber tip was separated from the gel surface by 0.5 mm and the distance between the fiber tip and the hydrophone tip was 2 mm. The drilling depth and the crater diameter were measured directly from the flash videographs.

Fresh human menisci were used to perform underwater laser cuts *in vitro*. The tissue samples were obtained after surgical extraction and studied after 1 to 4 weeks of freezing at $-20°C$. Prior to use, the tissue samples were kept moist in saline-soaked gauze and allowed to equilibrate to room temperature. The cuts were performed with laser pulse energies of 1 and 200 mJ for the Ho:YAG and the Er:YAG lasers, respectively. The pulse duration for both wavelengths was 400 μs. The tissue-containing cuvette was fixed on an x-y-z-translation stage to maintain a constant cutting velocity of 0.54 mm/s, resulting in a 50% overlap (short diameter) of the elliptical laser spot on the tissue surface between two consecutive laser pulses. Cuts were performed parallel to the optical fiber axis. After laser irradiation, the tissue was fixed in formalin, decalcified in ethylene diamine tetraacetic acid (EDTA), embedded in paraffin, and sectioned for histological analysis (hematoxylin-eosin staining). The tissue damage adjacent to the laser-induced crater was evaluated using light microscopy and polarization (birefringence) microscopy.

3 RESULTS

3.1 BEAM PROPAGATION IN AIR

In air, both wavelengths are totally internally reflected at the angled surface if the angle of incidence exceeds the angle of total reflection. Then the beam propagates sideways, as indicated by the shaded area in Figure 1. Total internal reflection at the angled surface is achieved for 2.12- and 2.94-μm rays at angles of incidence larger than 44.5 deg. For the totally reflected beam propagating in a plane perpendicular to the fiber axis, the fiber itself acts as a cylindrical lens, generating a focus at a distance 720 μm from the lateral fiber tip. The calculated divergence angle of the beam in the plane perpendicular to the fiber axis amounted to $\alpha = 17$ deg. In the axial direction, no lensing appears and the beam divergence is given by the numerical aperture of the fiber ($\beta = 11.5$ deg).

Figure 3(a) shows a schematic of the beam propagation in air. The diameter of the impact pattern produced by the Er:YAG laser beam on absorbing paper at different positions along the laser beam propagation is shown in Figure 3(b). The angle of a ray propagating in the fiber in the axial direction was 44 deg as calculated using geometric optics [see Figure 3(a), bold solid line in the z direction). In using the fiber delivery system in a water medium, however, the index of refraction changes and the radiation leaves the fiber in a forward (axial) direction (see Figure 1).

3.2 BEAM PROPAGATION IN WATER

Typical results from the He:Ne laser transmission experiments with the side-firing tip submerged are shown in Figure 4(a) for the Ho:YAG and in Figure 4(b) for the Er:YAG laser. The upper trace of Figure 4(a) shows the temporal intensity profile of an Ho:YAG laser pulse with a pulse energy of $E = 43$ mJ. The He:Ne laser beam signal is shown in the middle trace, and the pressure signal measured with the needle hydrophone in water is in the lower trace. During the first 240 μs of the Ho:YAG laser pulse, the He:Ne laser signal stays maximum, indicating that up to this time no vapor bubble had been formed. At $\Delta t = 240$ μs, the signal starts to decrease. After about 460 μs, it rises again to reach the original value at about 600 μs. The fraction of the laser pulse energy ΔE delivered until the moment when the He:Ne beam became deflected was measured for three different laser pulse energies (182, 85, and 43 mJ) to be 35.8 ± 1.2 mJ, resulting in a bubble formation threshold of $H_{Ho} = 6.3 \pm 0.2$ J/cm^2
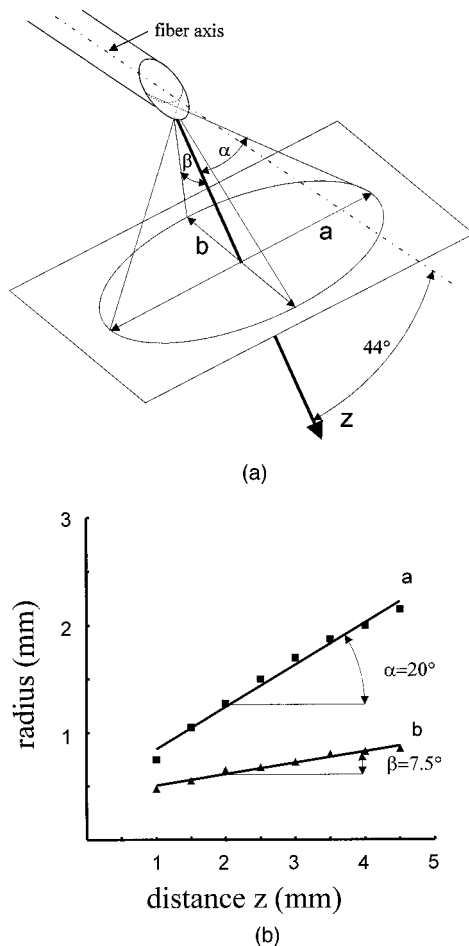
(a)

(b)

Fig. 3 (a) Schematic of the beam propagation in air and (b) beam diameters measured from impacts of an Er:YAG laser pulse ($E = 46$ mJ) on an absorbent photo paper as a function of the distance z from the fiber tip.

(a)

(b)

Fig. 4 Typical sequences of the transmission experiment with He:Ne laser radiation for (a) Ho:YAG and (b) Er:YAG laser pulses. Upper trace, temporal intensity profile of the laser pulse; middle trace, He:Ne photodiode signal; and lower trace, pressure transient measured with the needle hydrophone. Note the temporal correlation of the He:Ne-diode signal and the pressure transients in Figure 4(b).

at the fiber end surface ($A = 5.6 \times 10^{-3}$ cm^{-2}). At $\Delta t = 500$ μs after the beginning of the Ho:YAG laser pulse ($E = 43$ mJ), a pressure transient with an amplitude in the range of 9 bar was measured.

Figure 4(b) shows the temporal intensity of an Er:YAG laser pulse ($E = 3$ mJ) and the corresponding He:Ne and pressure signals. At $\Delta t = 100$ μs, the diode signal decreases for the first time, indicating a deflection of the He:Ne laser beam. The radiant exposure H_{Er} until the moment when the He:Ne beam was deflected sideways was measured for three different pulse energies (2.6, 3, and 4 mJ) to be 0.2 ± 0.04 J/cm^2. At $\Delta t = 170$ μs, the intensity of the deflected He:Ne beam rises to a first relative maximum. For the specific laser pulse energy of 3 mJ, this cycle was repeated four times during the laser pulse length of 400 μs [see middle trace of Figure 4(b)]. Each cycle was accompanied by the appearance of a pressure transient detected by the hydrophone. The pressure amplitudes amounted to about 4 bar. For Er:YAG laser pulse energies higher than 14 mJ, the He:Ne laser signal was found to follow the temporal profile of the laser pulse: it was de-
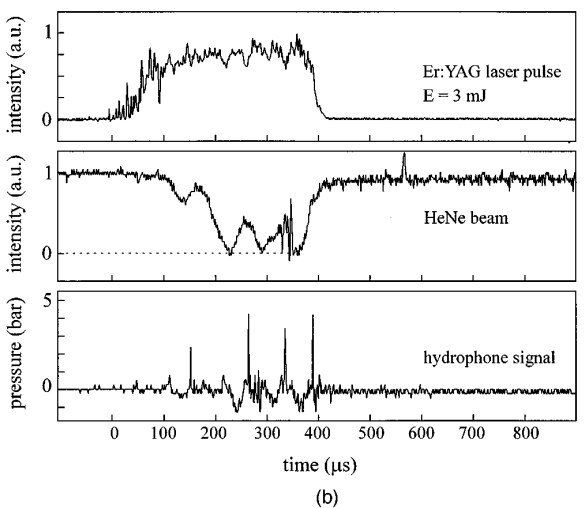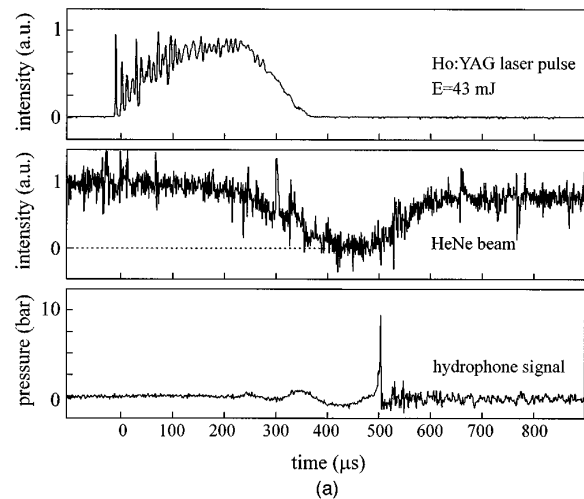
flected almost simultaneously with the beginning of the laser pulse and reached the original value not later than 100 μs after the end of the laser pulse.[25]

3.3 DYNAMICS OF BUBBLE FORMATION

A sequence of pictures of the vapor bubble formation taken at different times during an Ho:YAG laser pulse ($E = 700$ mJ) is shown in Figure 5. The schlieren imaging technique visualizes the heated water in front of the fiber due to the temperature-dependent changes of the index of refraction. The sideview pictures of the side-firing tip show that until $\Delta t = 20$ μs, the radiation leaves the fiber only in an axial direction and heats the water without forming a vapor bubble. At $\Delta t = 30$ μs, the first sign of the development of a vapor bubble at the angled surface (black arrow) is visible. Due to the change
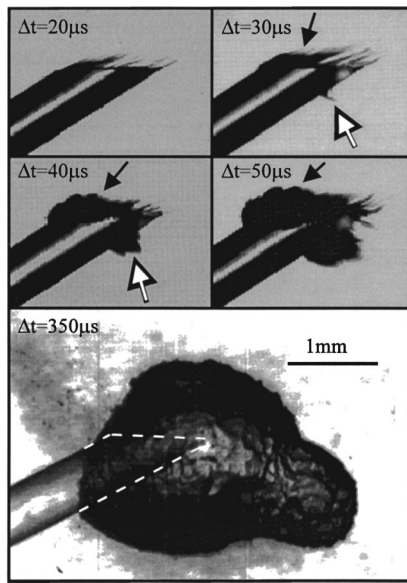
Fig. 5 Schlieren optical pictures of the bubble formation process induced by an Ho:YAG laser pulse ($E = 700$ mJ, $\tau = 400 \ \mu$s). The time delays Δt with respect to the beginning of the laser pulse are printed in the upper left corner of each picture. The black arrows indicate a vapor bubble at the angled surface and the white arrow the start of a bubble formation sideways to the fiber.

Fig. 6 Frontal illuminated pictures of the bubble formation process induced by an Er:YAG laser pulse ($E = 200$ mJ, $\tau = 400 \ \mu$s). The time delays Δt with respect to the beginning of the laser pulse are printed in the upper left corner of each picture. Figure 6(a) shows the angled surface with microbubbles. The other figures show the bubble formation process in side view. Note the thin vapor layer at the angled surface until $\Delta t = 100 \ \mu$s, marked by the black arrows.

in the index of refraction from water to water vapor, the distal fiber tip surface serves as a total reflector. Therefore, part of the radiation becomes reflected to the side of the fiber and is visualized by the dark streaks (white arrow). At $\Delta t = 40 \ \mu$s, the bubble starts to grow in a sideways direction. The picture taken at $\Delta t = 50 \ \mu$s shows a vapor bubble growing in an axial and sideways direction. At its maximum size ($\Delta t = 350 \ \mu$s after the start of the laser pulse), the bubble is pear shaped and has covered the entire fiber tip. The largest extension of about 1.9 mm is found at an angle of 44 deg with respect to the fiber axis.

The development of a vapor bubble generated by an Er:YAG laser pulse ($E = 200$ mJ) is shown in Figure 6. The view onto the distal surface of the angled fiber [Figure 6(a) at $\Delta t = 10 \ \mu$s] reveals the generation of randomly distributed microbubbles. In the side-view picture, the formation of a microbubble beside the fiber is recognizable [white arrow in Figure 6(b) at $\Delta t = 10 \ \mu$s]. At $\Delta t = 20 \ \mu$s, a thin vapor layer had been formed throughout the angled surface (black arrow) and the start of a vapor bubble on the side of the fiber tip (white arrow) is clearly visible. The initial vapor layer at the angled surface stayed open during the entire duration of the laser pulse. At $\Delta t = 100 \ \mu$s, an elongated, cigarlike channel was formed in a sideways direction (at 44 deg relative to the fiber axis) that partially covered the angled surface. The channel reached its maximum size at the end of the 400-μs long laser pulse.

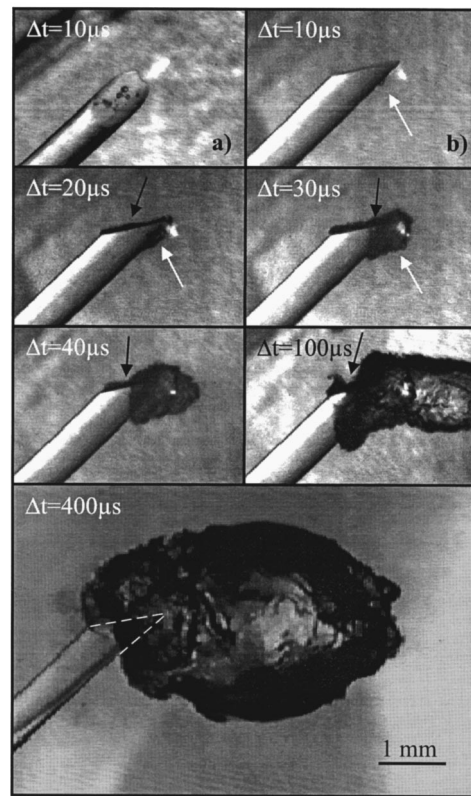The maximum depth of the bubble defined in a direction perpendicular to the fiber axis is shown as

a function of the laser pulse energy in Figure 7 for Ho:YAG and Er:YAG laser pulses. The maximum depth was reached at a delay of 350 and 400 μs (with respect to the beginning of the laser pulse) for the Ho:YAG and the Er:YAG lasers, respectively. The solid curve represents the logarithmic least-square fit to the measured values. The values for the threshold of bubble formation determined from the intercepts of the least-square fits correlate well with the energy values ($E_{Ho} = 35.8 \pm 1.2$ mJ and $E_{Er} = 1.1 \pm 0.2$ mJ) determined in a separate experiment using the He:Ne transmission method.

The maximum amplitude of the pressure signal measured during the collapse of the vapor bubble is presented in Figure 8 as a function of the laser pulse energy for both laser wavelengths. For the Ho:YAG laser, the graph reveals an increase in the amplitude of collapse pressure with increasing laser pulse energy up to energies of about 170 mJ. For higher pulse energies, only a slight increase (slope of 0.12 bar/J) was detectable. For the Er:YAG laser, the amplitude of collapse pressure increased almost linearly (2.5 bar/J) over the entire energy range measured. Except for Er:YAG laser pulse energies below 14 mJ, where multiple transients were found
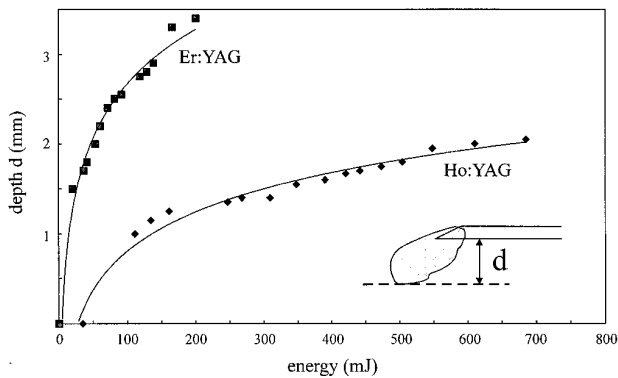
Fig. 7 Depth of the vapor channel at the submerged side-firing tip vs. pulse energy. The laser pulse length was $\tau = 400$ μs. The thresholds for bubble formation (open symbols at $d = 0$ mm) were separately determined by the He:Ne transmission experiment to be $E_{Ho} = 35.8 \pm 1.2$ mJ and $E_{Er} = 1.1 \pm 0.2$ mJ.

Fig. 8 Maximum pressure amplitude at the collapse center during the collapse of the vapor bubble at the submerged side-firing tip vs. pulse energy. Laser pulse length $\tau = 400$ μs. The pressure amplitude was calculated assuming a $1/r$ dependence of a spherical wave.

during the pulse [see Figure 4(b)], the pressure transient for all the other pulse energies occurred after the end of the 400-μs laser pulse.[26] It is remarkable that the maximum amplitude measured during the collapse of a bubble that was produced with Er:YAG laser pulses of energies higher than 100 mJ was always larger than after the collapse of an Ho:YAG laser-generated bubble.

3.4 TISSUE TREATMENT

The videographs in Figure 9 show the impacts of laser pulses on poly(acrylamide) gel under water. The angle between the horizontal plane and the fiber axis was chosen as 46 deg in order to drill holes perpendicular to the gel surface. Figure 9(a) shows the impact of an Ho:YAG laser pulse on the gel using a pulse energy of 200 mJ. The picture taken at
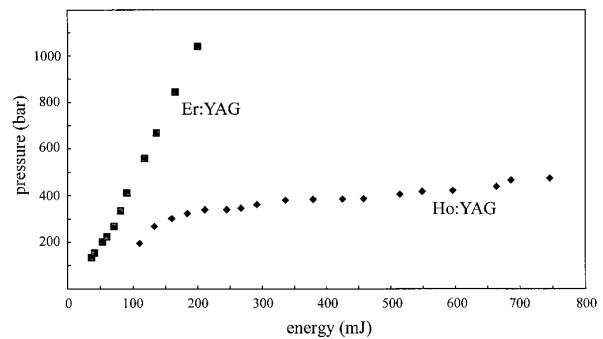
350 μs after the beginning of the laser pulse shows the maximum dimension of the vapor bubble. The bubble between the fiber tip and the gel surface is almost spherical. In the gel, hardly any impact was visible.

In Figure 9(b), the Ho:YAG laser pulse energy was 1 J. With this pulse energy, the maximum channel depth in the gel was 1.15 mm. The amplitude of the pressure generated during the subsequent collapse of the vapor bubble amounted to $p_{Ho} = 131$ bar± 45 bar. Since the symmetry of the water flow around the fiber was strongly perturbed by the sample surface, the pressure amplitude was only about half of that generated by an undisturbed bubble (see Figure 8).

Figure 9(c) shows the impact of an Er:YAG laser with a pulse energy of 200 mJ. The delay of the illuminating flashlamp was 400 μs, which corresponded to the maximum depth of the impact. The
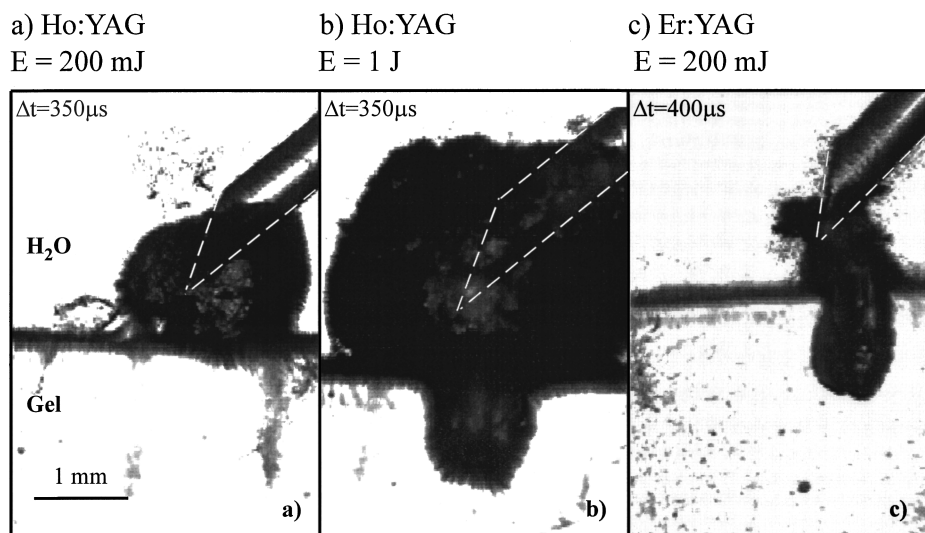

Fig. 9 Videographs of underwater laser impacts on a poly(acrylamide) gel (water concentration of 80%). The distance between the fiber tip and the gel surface was 0.5 mm.
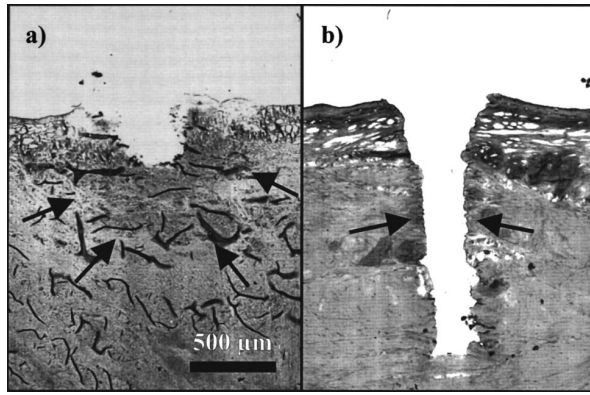
Fig. 10 Histological sections of human menisci after underwater laser cuts with (a) Ho:YAG laser pulses of $E = 1000$ mJ and (b) Er:YAG laser pulses of $E = 200$ mJ. The cuts were performed by moving the fiber five times parallel to the fiber axis. The distance between the fiber tip and the tissue was 0.5 mm. The extent of the thermally damaged tissue is marked by arrows.

drilling depth into the gel was 1.1 mm. The amplitude of the subsequent collapse pressure amounted to $p_{Er} = 101$ bar ± 13 bar. It is remarkable that the amplitude of the pressure signal generated during the collapse of the Er:YAG bubble was almost as high as during the collapse of the Ho:YAG bubble, although the latter had a much larger volume [compare Figures 9(b) and 9(c)].

Based on the results obtained from the laser treatment of a gel, the laser pulse energies chosen for the treatment of human menisci were 1J and 200 mJ for the Ho:YAG and the Er:YAG lasers, respectively. Histological sections of human menisci after Ho:YAG laser irradiation are shown in Figure 10(a) and after Er:YAG laser irradiation in Figure 10(b). The pictures show cuts performed by moving the fiber five times (back and forth) over the tissue sample in a direction parallel to the fiber axis. The crater depth of the Ho:YAG laser impact was 360 μm. A zone of thermally altered tissue (400 ± 200 μm) can be recognized for the Ho:YAG laser cuts [indicated by arrows in Figure 10(a)]. The crater depth of the Er:YAG laser impacts was 1300 μm,

with a zone of thermally altered tissue of 60 ± 10 μm along the crater wall [indicated by arrows in Figure 10(b)]. In a wide range of radiant exposures (Er:YAG, 30 to 170 J/cm^2; Ho:YAG, 400 to 1500 J/cm^2), the extent of damaged meniscal tissue around the crater wall after laser impact was found to be a constant 50 ± 20 μm (Er:YAG) and 500 ± 300 μm (Ho:YAG).

3.5 FIBER DAMAGE

The scanning electron microscopy pictures of two different side-fire fiber tips (low OH, fiber core diameter of 540 μm) damaged during the study are shown in Figure 11. The fiber tip in Figure 11(a) was damaged after delivery of 20 laser pulses (pulse energy of 500 mJ) into the water-filled cuvette. The distal tip of the side-fire fiber was broken and quartz fragments were splintered off. A chronological sequence of photographs taken during the bubble formation process revealed that the collapse center of the vapor bubble that was almost spherically centered around the tip of the fiber was located directly at the fiber tip. In contrast to the clearly mechanically damaged fiber tip after Ho:YAG laser treatment, the fiber damage after Er:YAG radiation [Figure 11(b)] seems to be more likely induced by ablation. The cuts in meniscus with the Er:YAG laser radiation were performed with the fiber tip shown in Figure 11(b). About 17,000 laser pulses with a pulse energy of 200 mJ were applied. The rough half-circle surface beside the fiber shows the exit area of the side-fire fiber (indicated by arrows).

4 DISCUSSION

The purpose of this study was to evaluate the feasibility of a side-firing delivery system for Ho:YAG and Er:YAG laser radiation in view of applications in orthopedic surgery. A fundamental knowledge of the optical principles when radiation exits an angled fiber tip could be acquired by using different imaging techniques, pressure measurements, and He:Ne laser transmission experiments. Since
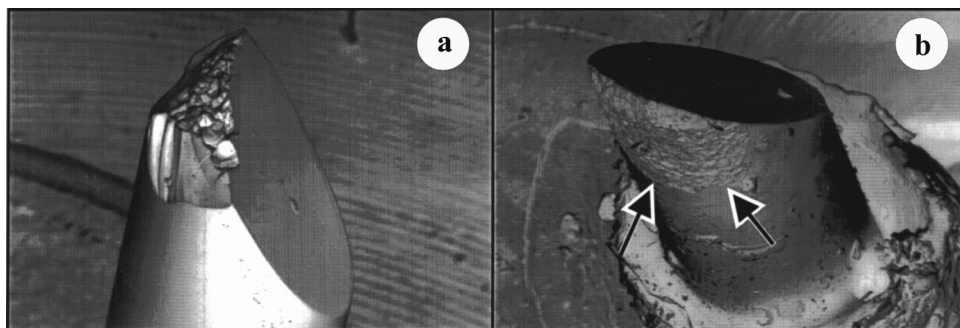

Fig. 11 SEM micrographs of a side-firing fiber tip after laser treatment. (a) 20 Ho:YAG laser pulses fired into a water-filled cuvette ($E = 500$ mJ, $\tau = 400$ μs) and (b) 17,000 Er:YAG laser pulses ($E = 200$ mJ, $\tau = 400$ μs) used for underwater cutting of meniscus (outer diameter of the fiber, 600 μm).

the generation of vapor bubbles at a submerged fiber is essential for tissue ablation with IR radiation under water, the initial bubble formation process and the bubble dynamics were investigated. The difference in the absorption coefficients for 2.12- and 2.94-μm laser radiation in water was found to be responsible for the different bubble dimensions and the different tissue effects induced by comparable laser parameters.[27]

4.1 BEAM PROPAGATION AT THE SIDE-FIRE FIBER TIP AND BUBBLE FORMATION

Beam propagation at the side-firing fiber tip is equal for both the Ho:YAG laser wavelength at 2.12 μm and the Er:YAG laser wavelength at 2.94 μm since the indices of refraction in quartz and water for both wavelengths are similar (see Table 1).

If the fiber tip is submerged in water, the mismatch of the indices of refraction is much smaller than in air, allowing the radiation to outcouple in a forward direction. Since Ho:YAG and Er:YAG laser radiation is strongly absorbed in water, the first part of a laser pulse evaporates a water layer at the angled fiber surface, forming a vapor bubble[28] (Figures 5 and 6). This vapor bubble induces an impedance jump comparable to that in air and thus the remaining part of the laser pulse becomes totally reflected and exits the fiber tip sideways. The amount of pulse energy necessary to establish such a vapor bubble, however, depends strongly on the absorption coefficient μ_a of each wavelength in water.

Owing to the 300-fold lower absorption coefficient of Ho:YAG laser radiation compared with Er:YAG radiation, the energy is deposited in a much larger volume given by the optical penetration depth and the area of the angled surface of the fiber. Therefore more Ho:YAG laser energy is required for bubble formation. Given the same rate of energy deposition for both lasers, it takes more time for the Ho:YAG laser until the bubble formation starts. The big difference in the time between the start of the laser pulse and the first sign of bubble formation is impressively shown in Figure 4. Although the rate of energy deposition of the Ho:YAG radiation is about ten times higher than the Er:YAG radiation, the delay time is more than double. The difference in absorption is also apparent in the higher threshold for bubble formation for the Ho:YAG laser wavelength ($H_{Ho} = 6.3$ J/cm^2) compared with the Er:YAG wavelength ($H_{Er} = 0.2$ J/cm^2). Our measurements of the ablation threshold using the deflection of the He:Ne laser beam resulted in values that are about two times smaller than those reported in the literature,[29,30] which were evaluated with pump-probe or imaging techniques. The reason for the difference is that our measurements determined the lowest radiant exposure at which the first change in the index of refraction at the distal fiber tip occurs.

With a bare fiber, the low optical penetration depth of 2.94 μm in water has been shown to cause the generated vapor bubble to collapse during the duration of the laser pulse.[15,31] This behavior was also observed with a submerged side-firing fiber if the energy of the 400-μs-long Er:YAG pulse was below 14 mJ, as shown in Figure 4(b). Images have shown that in this case the bubble created at the angled fiber tip does not coalesce with the sideways bubble. As soon as a vapor bubble has been formed at the angled fiber surface, all the laser radiation becomes reflected sideways and therefore no longer contributes to maintaining the vapor bubble in an axial direction. As a consequence, the bubble collapses and the radiation leaves the fiber again in forward direction, forming a new bubble. Each collapse is accompanied by the generation of a pressure transient [see Figure 4(b)]. These pressure transients were generated some 10 μs after a local minimum of the He:Ne diode signal. This delay indicates that the vapor bubble became separated from the fiber tip before it collapsed. The diode signal does not rise to a maximum value because the He:Ne radiation is scattered at the remaining bubble in front of the angled surface and/or is deflected at a new vapor bubble induced by the remaining pulse energy. The cycle of bubble generation and collapse is repeated up to four times during the pulse duration.

For Er:YAG pulses with an energy larger than 14 mJ, the rate of energy deposition of the 400-μs pulse is high enough to cause the fast-growing sideways bubble to coalesce with the thin vapor layer formed at the angled surface [see Figure (6) at $\Delta t = 40$ μs]. Owing to the large beam divergence of 17 deg, in the plane perpendicular to the fiber axis, a result of the cylinder lens (see Figure 3), the diameter of the bubble is much larger than with a bare fiber. Unlike the elongated cylindrical (cigar-shaped) form of a vapor bubble generated with a bare fiber,[32] the form of the sideways bubble is more egg-shaped or even spherical as shown in Figure 6. As a result of the more spherical shape of the vapor bubble, the sideways bubble does not collapse during the pulse duration in contrast to a bubble generated with the same laser parameters and a bare fiber.[15]

On the other hand, the amplitude of the pressure transient generated during the collapse of a vapor bubble is higher the more spherical the shape of the bubble.[17] In fact, the pressure recorded at the collapse of a sideways (egg-shaped) bubble generated with the Er:YAG laser was found to be almost twice that measured during the collapse of the elongated cylindrical bubble generated with a bare fiber.[16]

In contrast, owing to the more than 300-fold larger optical penetration depth of Ho:YAG laser radiation compared with Er:YAG radiation, a larger and more spherical vapor bubble is formed at the angled surface of the fiber. This bubble was found to coalesce with the sideways-formed bubble, even

with low pulse energies. The resulting shape of the bubble at the submerged side-firing tip was similar to the shape of the bubble formed at a bare fiber tip[33] (Figure 5).

For a given pulse energy, the collapse pressure amplitudes generated at a bare fiber tip were found to be always higher for Ho:YAG laser radiation than for Er:YAG radiation. Contrary to this, this study revealed that the amplitude of the collapse pressure of a bubble generated at a side-firing fiber is higher for the Er:YAG laser than for the Ho:YAG laser. The reason for this again is found in the different geometry and dynamics of the bubble. Although the sizes of the Ho:YAG ($E = 700$ mJ) and Er:YAG ($E = 200$ mJ) laser-generated bubbles are comparable, the location of the fiber tip in relation to the bubble is different (compare Figure 5 and 6). A chronological sequence of photographs showed that the Ho:YAG laser bubble collapsed with its collapse center located directly at the fiber tip. The fiber thereby strongly damped the collapse. As a result of the laser-induced pressure wave, parts of the fiber tip can splinter as shown in Figure 11(a).

In contrast, the Er:YAG bubble separated from the fiber tip during the collapse. Although this led to a higher amplitude of collapse pressure (Figure 8), it avoided mechanical damage to the fiber tip. After Er:YAG laser treatment the main damage mechanism, caused by the high absorption coefficient of water and water containing tissue, was a successive abrasion of the fiber tip [see Figure 11(b)].

For both laser wavelengths, although the lifetime of the vapor bubble was longer for the Ho:YAG laser, the radiation was found to be shorter than 1 ms. This means that during the intervals between two consecutive laser pulses the continuous-wave radiation of the He:Ne laser, which is used as an aiming beam, points forward and not in the sideways direction where the Er:YAG or Ho:YAG laser radiation will hit the tissue. Therefore the aiming beam does not indicate where the surgeon will irradiate the tissue. Assuming a repetition rate of 20 Hz and a laser pulse length of 400 μs, the He:Ne beam is totally reflected with a duty cycle of less than 1/100 per second in a sideways direction that is not long enough for the human eye to see. Furthermore, the irregular bubble wall reflects and scatters the visible radiation, and the aiming beam will not illuminate the spot where the Ho:YAG or Er:YAG radiation will be deposited. Hence, a clinical side-firing fiber device should be either HR-coated for the aiming beam wavelength at the angled fiber surface or produced in such a way that a permanent vapor bubble is melted into the fiber tip.

4.2 TISSUE TREATMENT

Bubble formation at the fiber tip is necessary for underwater tissue treatment in order to bridge the distance of typically 0.5 to 1 mm between the fiber tip and the tissue surface. Since the absorption of 2.12- and 2.94-μm radiation in steam is negligible, direct tissue irradiation through the vapor bubble is possible.[14] In Figure 9 it is shown that tissue perpendicular to the fiber axis can be treated because the radiation propagates at an angle of 44 deg sideways to the angled fiber tip. A comparison of Figures 9(a) and 9(c) clearly illustrates the difference in ablation efficiency of Ho:YAG and Er:YAG laser radiation. Although the same pulse energy of 200 mJ was used, the Er:YAG laser was able to drill a hole in the tissue phantom whereas almost the whole Ho:YAG laser pulse energy was used in bridging the water between the fiber tip and the gel surface. To produce a comparable crater depth in the gel (≈ 1 mm), an Er:YAG laser pulse with an energy of 200 mJ and an Ho:YAG laser with an energy of $E = 1$ J were required.

The fivefold higher pulse energy of the Ho:YAG laser leads to the generation of a vapor bubble several times larger than that of the Er:YAG laser pulse. It is known that the collapse pressure amplitude is lower the more asymmetric and disturbed the dynamics of the collapse.[34] The pressure amplitude generated during the collapse, however, was found to be comparable for both lasers. We speculate that since the fiber tip is totally enfolded, it affects the collapse of the Ho:YAG bubble much more than the collapse of the Er:YAG bubble. In addition, it was found that as a result of the lower absorption coefficient of Ho:YAG laser radiation in water, the temperature gradient at the vapor bubble–water interface is much lower for the Ho:YAG bubble than for the Er:YAG bubble.[27] Therefore the rate at which molecules condense at the bubble wall is lower, which leads to slower collapse dynamics of the Ho:YAG bubble. The bubble collapse is also disturbed by the evaporated and ablated tissue particles, which damp the collapse amplitudes.[35,36]

The influence of the absorption coefficient on tissue ablation efficiency and tissue damage is also illustrated by the histological microsections of menisci after Ho:YAG and Er:YAG laser irradiation (Figure 10). Although the Ho:YAG pulse energy is five times higher than that of the Er:YAG laser, the tissue crater is only a third as deep (360 μm versus 1300 μm).

Although the pressure measurements revealed the existence of high-pressure transients (several hundred bar) during bubble collapse that can damage the fiber tip, the histology did not show any sign of mechanically induced tissue damage. It is, however, possible that pressure-induced tissue damage may cause a delayed response that is only visible in an *in vivo* experiment. On the other hand, bubble expansion has been identified as the source of the dissections found in vascular tissue after Ho:YAG laser impact.[37,38] It is therefore more likely

that the bubble dynamics exhibit a higher potential for mechanical tissue damage than the collapse pressure wave when the laser is applied in the narrow operation field of a joint. Since the bubble size depends on both the radiation exposure and the geometry of the operation, the pulse energy and the fiber tissue distance should be kept as small as possible to minimize the risk of mechanical tissue damage.

5 CONCLUSIONS

The results of this study show that a side-firing fiber delivery device for endoscopic applications for Ho:YAG and Er:YAG laser radiation is feasible for treating tissue in a liquid environment. In underwater operations, the leading part of the laser pulse generates a vapor bubble at the angled surface of the fiber, and the side-firing tip works in the same way as it does in air. The sideways beam propagation of the 30-deg side-firing fiber tip induces bubble formation at an angle of 44 deg to the fiber axis. Therefore underwater tissue treatment in a narrow operation field is possible.

Furthermore, our systematic study of laser-induced pressure transients and tissue effects suggests that there is the least potential for mechanical tissue damage when the radiation exposure is reduced and the distance between the fiber tip and the tissue surface is minimized to keep the bubble size small. *In vivo* investigations are required to prove whether the fiber delivery system meets the clinical reality.

Acknowledgments

REFERENCES

1. J. A. Curcio and C. C. Petty, ''The near infrared absorption spectrum of liquid water,'' *J. Opt. Soc. Am.* **41**, 302–304 (1951).
2. V. M. Zolotarev, B. A. Mikhailov, L. I. Alperovich, and S. I. Popov, ''Dispersion and absorption of liquid water in the infrared and radio regions of the spectrum,'' *Opt. Spectrosc.* **27**, 430–432 (1969).
3. G. S. Fanton and M. F. Dillingham, ''The use of the holmium: YAG-laser in arthroscopic surgery,'' *Semin. Orthop.* **7**, 102–116 (1992).
4. H. Pratisto, M. Frenz, M. Ith, V. Romano, D. Felix, R. Grossenbacher, H. J. Altermatt, and H. P. Weber, ''Temperature and pressure effects during erbium laser stapedotomy,'' *Lasers Surg. Med.* **18**, 100–108 (1996).
5. J. M. Krauss and C. A. Puliafito, ''Lasers in ophthalmology,'' *Lasers Surg. Med.* **17**, 102–159 (1995).
6. M. Kautzy, M. Susani, and P. Schenk, ''Holmium:YAG Infrarot Laser und UV-Excimer. Laser Effekte auf orale Schleimhautgewebe,'' *Laryngorhinootologie* **71**, 347–352 (1992).
7. S. Spörri, M. Frenz, H. J. Altermatt, H. U. Bratschi, V. Romano, M. Forrer, E. Dreher, and H. P. Weber, ''Effects of various laser types and beam transmission methods on female organ tissue in the pig: an *in vitro* study,'' *Lasers Surg. Med.* **14**, 269–278 (1994).
8. C. Deuerling, W. Prettl, M. Nuebler-Moritz, H. Niederdellmann, P. Hering, W. Falkenstein, and B. Rückle, ''Transmission systems for the Er:YAG laser—state of the art,'' in *Lasers in Medicine*, W. Waidelich, G. Staehler, and R. Waidelich, eds., pp. 548–551, Springer Verlag, New York (1995).
9. I. Gannot, S. Schründer, J. Dror, A. Inberg, T. Ertl, J. Tschepe, G. J. Müller, and N. Croitoru, ''Flexible waveguides for Er-YAG laser radiation delivery,'' *IEEE Trans. Biomed. Eng.* **42**, 967–972 (1995).
10. J. A. Harrington, ''Laser power delivery in infrared fiber optics,'' *Proc. SPIE* **1649**, 14–22 (1992).
11. D. Helfer, M. Frenz, V. Romano, and H. P. Weber, ''Fiber-end micro-lens system for endoscopic erbium-laser surgery applications,'' *Appl. Phys. B* **58**, 309–315 (1994).
12. M. Buchelt, T. Papaioannou, M. Fishbein, W. Peters, C. Beeder, and W. S. Grundfest, ''Excimer laser ablation of fibrocartilage: an *in vitro* and *in vivo* study,'' *Lasers Surg. Med.* **11**, 271–279 (1991).
13. M. Ith, H. Pratisto, H. U. Stäubli, H. J. Altermatt, M. Frenz, and H. P. Weber, ''Side effects of laser therapy on cartilage,'' *Sports Exercise Injury* **2**, 207–209 (1996).
14. T. G. van Leeuwen, M. J. van der Veen, R. M. Verdaasdonk, and C. Borst, ''Non-contact tissue ablation by holmium: YSGG laser pulses in blood,'' *Lasers Surg. Med.* **11**, 26–34 (1991).
15. M. Ith, H. Pratisto, H. J. Altermatt, M. Frenz, and H. P. Weber, ''Dynamics of laser-induced channel formation in water and influence of pulse duration on the ablation of biotissue under water with pulsed erbium laser radiation,'' *Appl. Phys. B* **59**, 621–629 (1994).
16. M. Frenz, H. Pratisto, M. Ith, K. Rink, G. Delacrétaz, V. Romano, R. P. Salathé, and H. P. Weber, ''Transient photoacoustic effects induced in liquids by pulsed erbium laser,'' *Proc. SPIE* **2134**, 402–412 (1994).
17. E. D. Jansen, T. Asshauer, M. Frenz, M. Motamedi, G. Delacrétaz, and A. J. Welch, ''Effect of pulse duration on bubble formation and laser-induced pressure waves during holmium laser ablation,'' *Lasers Surg. Med.* **18**, 278–293 (1996).
18. C. D. Ohl, A. Phillip, and W. Lauterborn, ''Cavitation bubble collapse studied at 20 million frames per second,'' *Ann. Phys.* **4**, 26–34 (1995).
19. O. Föhn, ''Power maximization and wavelength-selection of flash lamp pumped erbium lasers in the $3\mu m$ region,'' *Technical Report*, Institute of Applied Physics, Bern (1996).
20. H. Pratisto, M. Frenz, F. Könz, H. J. Altermatt, and H. P. Weber, ''Combination of erbium and holmium laser radiation for tissue ablation,'' *Proc. SPIE* **2681**, 201–206 (1996).
21. D. Helfer, ''Endoscopic beam delivery systems for erbium laser radiation,'' Master's Thesis, Lasers Department, University of Berne (1993).
22. H. Schoeffmann, H. Schmidt-Kloiber, and E. Reichel, ''Time-resolved investigations of laser-induced shock waves in water by use of polyvinylideneflouride hydrophones,'' *J. Appl. Phys.* **63** (1988).
23. R. Hickling and M. S. Plesset, ''Collapse and rebound of a spherical bubble in water,'' *Phys. Fluids* **7**, 7–14 (1964).
24. T. Asshauer, G. Delacrétaz, E. D. Jansen, A. J. Welch, and M. Frenz, ''Pulsed holmium laser ablation of tissue phantoms: correlation between bubble formation and acoustic transients,'' *Applied Phys B* **65**, 647–657 (1997).
25. F. Könz, M. Frenz, H. Pratisto, H. P. Weber, A. S. Silenok, and V. I. Konov, ''Starting mechanisms of bubble formation induced by Ho:Tm:YAG laser in water,'' *Proc. SPIE* **2624**, 67–71 (1995).
26. F. Könz, O. Föhn, H. Pratisto, M. Frenz, and H. P. Weber, ''Side-firing fiber for tissue ablation with erbium laser under water,'' *Proc. SPIE* **2681**, 226–232 (1996).
27. M. Frenz, H. Pratisto, F. Könz, E. D. Jansen, A. J. Welch, and H. P. Weber, ''Comparison of the effects of absorption coefficient and pulse duration of 2.12 μm and 2.79 μm radiation on laser ablation of tissue,'' *IEEE-JQE* **32**, 2025–2036 (1996).
28. H. Loertscher, W. Q. Shi, and W. S. Grundfest, ''Tissue ab-

lation through water with erbium: YAG lasers,'' *IEEE Trans. Biomed Eng.* **39**, 86–87 (1992).

29. K. T. Schomacker, Y. Domankevitz, T. J. Flotte, and T. F. Deutsch, ''Co:MgF2 laser ablation of tissue: effect of wavelength on ablation threshold and thermal damage,'' *Lasers Surg. Med.* **11**, 141–151 (1991).

30. Y. Domankevitz, M. S. Lee, and N. S. Nishioka, ''Pulsed holmium laser tissue ablation threshold studies,'' *Proc. SPIE* **1646**, 42–45 (1992).

31. H. Pratisto, M. Frenz, M. Ith, H. J. Altermatt, E. D. Jansen, and H. P. Weber, ''Combination of fiberguided pulsed erbium and holmium laser radiation for tissue ablation under water,'' *Appl. Opt.* **35**, 3328–3337 (1996).

32. H. Pratisto, M. Ith, M. Frenz, and H. P. Weber, ''Infrared multiwavelength laser system for establishing a surgical delivery path through water,'' *Appl. Phys. Lett.* **67**, 1963–1965 (1995).

33. T. Asshauer, K. Rink, G. Delacrétaz, R. P. Salathé, B. Gerber, M. Frenz, H. Pratisto, M. Ith, V. Romano, and H. P. Weber, ''Acoustic transient generation in pulsed holmium laser ablation under water,'' *Proc. SPIE* **2134**, 423–433 (1994).

34. A. Vogel and W. Lauterborn, ''Acoustic transient generation by laser-produced cavitation bubbles near solid boundaries,'' *J. Acoust. Soc. Am.* **84**, 719–731 (1988).

35. T. Asshauer, T. Jansen, T. Oberthur, G. Delacrétaz, and B. E. Gerber, ''Holmium laser ablation of cartilage: effects of cavitation bubbles,'' *Proc. SPIE* **2391**, 379–385 (1995).

36. A. Vogel, R. Engelhardt, U. Behnle, and U. Parlitz, ''Minimization of cavitation effects in pulsed laser ablation—illustrated on laser angioplasty,'' *Appl. Phys. B* **62**, 173–182 (1996).

37. T. G. van Leeuwen, L. van Erven, J. H. Meertens, M. Motamedi, M. J. Post, and C. Borst, ''Origin of arterial wall dissections induced by pulsed excimer and mid-infrared laser ablation in the pig,'' *J. Am. Coll. Cardiol.* **19**, 1610–1618 (1992).

38. T. G. van Leeuwen, J. H. Meertens, E. Velema, M. J. Post, and C. Borst, ''Intraluminal vapor bubble induced by excimer laser pulse causes microsecond arterial dilation and invagination leading to extensive wall damage in the rabbit,'' *Circulation* **87**, 1258–1263 (1993).